BNL-212233-2019-JAAM

Rationalization of Diversity in Spinel MgFe2O4 Surfaces

H. Guo, P. Liu

To be published in "ADVANCED MATERIALS INTERFACES"

October 2019

Chemistry Department

Brookhaven National Laboratory

U.S. Department of Energy

USDOE Office of Science (SC), Basic Energy Sciences (BES) (SC-22)

DISCLAIMER

Rationalization of Diversity in Spinel $MgFe_2O_4$ Surfaces

*Haoyue Guo, Amy C. Marschilok, Kenneth J. Takeuchi, Esther S. Takeuchi, and Ping Liu**

H. Guo, Prof. A.-M. Marschilok, Prof. K.-J. Takeuchi, Prof. E.-S. Takeuchi, Dr. P. Liu
Department of Chemistry, Stony Brook University
Stony Brook, NY 11794, USA
E-mail: pingliu3@bnl.gov

Prof. A.-M. Marschilok, Prof. K.-J. Takeuchi, Prof. E.-S. Takeuchi
Department of Materials Science and Chemical Engineering, Stony Brook University
Stony Brook, NY 11794, USA

Prof. E.-S. Takeuchi
Energy Sciences Directorate, Brookhaven National Laboratory
Upton, NY 11793, USA

Dr. P. Liu
Chemistry Department, Brookhaven National Laboratory
Upton, NY 11793, USA

Keywords: $MgFe_2O_4$, ferrite, spinel, DFT, surface diagram

Abstract

Spinel magnesium ferrite ($MgFe_2O_4$) is a prospective anode material for lithium ion batteries (LIBs). Here, using density functional theory (DFT) we report the first systematic study of diverse $MgFe_2O_4$ surfaces in three types of spinel structures: normal, mixed, inverse, which can have significant impact on the initial lithiation. Our results show that the faceting and therefore the shape of $MgFe_2O_4$ crystals strongly depend on the bulk structures. Upon going from normal, mixed to inverse spinel, the energetically preferred facets of $MgFe_2O_4$ vary from the combination of (1 0 0) and (3 1 1), solely [1] to a combination of (1 0 0), (0 0 1), (1 1 1) and (3 1 1), respectively, depending on the distribution of Mg^{2+} in the spinel structure. However, there is one common descriptor to the stable surfaces among all three $MgFe_2O_4$ systems: high density of Mg^{2+} exposed to the surface. Our study rationalizes the essential effect of the substitution of Zn^{2+} for Mg^{2+} in ferrites and provides new insights on how to control the shape of ferrite materials and thus tune the performances of LIBs.

1. Introduction

Iron ferrites (AFe_2O_4) have been recognized as one of the promising electrode materials for lithium ion batteries (LIBs) due to their earth abundance, high lithium storage, facile preparation method and low toxicity.[2] These materials include zinc ferrite ($ZnFe_2O_4$) and magnesium ferrite ($MgFe_2O_4$). Previously, by employing density functional theory (DFT) we mapped the surface diagram of $ZnFe_2O_4$ and discovered the unique contributions of the surface facets to the initial lithiation, where Zn^{2+} ions are the key to generate active sites and facilitate the Li^+ ion intercalation via the facile displacement from 8a to 16c sites.[1, 2d, 3] In the present study, we move from $ZnFe_2O_4$ to $MgFe_2O_4$, aiming to understand the effect of substitution of Zn^{2+} for Mg^{2+} on the structures and the preferential surface orientations of the pristine spinel ferrite using DFT. Such mechanistic insight at the atomic level can be of great importance to extract the tuning principle and enable the design or optimization of spinel structures as LIBs electrode materials. We note, the lithium adsorption on these surfaces, transport from the surface to the subsurface and intercalation in the bulk, which are important to describe the lithiation behaviors, [1, 2d, 3-4], are beyond the interest of current effort and will be studied separately.

It has been reported that $MgFe_2O_4$ can adopt spinel structures in three forms. One is the normal-spinel with an oxygen-cubic-close-packed array (Figure 1a). Like $ZnFe_2O_4$[1, 2d, 3], the octahedral 16d sites are taken up by Fe^{3+} ions and O^{2-} ions are located at octahedral 32e sites, while all the 8a sites are occupied by Mg^{2+} rather than Zn^{2+} ions. In addition, the substitution of Zn^{2+} for Mg^{2+} can also enable the formation of $MgFe_2O_4$ via the mixed-spinel and inverse-spinel structures depending on the distribution of two metal cations between octahedral and tetrahedral sites.[5] The mixed and inverse spinel structures correspond to partial (Figure 1b) or complete (Figure 1c) intermixing of Mg^{2+} ions at the tetrahedral 8a sites and Fe^{3+} ions at the octahedral 16d in the normal-spinel structures. The degree of inversion, i as in (Mg_{1-}

$_{i}Fe_{i})_{8a}(Mg_{i}Fe_{2-i})_{16d}O_4$, depends on the synthesis details, such as calcination temperature and preparation method.[6]

The atomic structures and electronic properties of spinel electrode materials, such as Fe_3O_4 and $ZnFe_2O_4$ have been extensively studied using DFT.[1, 2d, 3, 7] Comparatively, little attention has been made to mixed-spinel $MgFe_2O_4$ due to its structural complexity, where only the simplified normal-spinel structure was studied.[8] In terms of the surface, to our best knowledge, only one theoretical study has been reported on the $MgFe_2O_4$(1 1 1) surface with a specific termination; yet the origin for such choice of surface orientation and structure, rather than many other possibilities was not addressed.[8d]

Here, the surface diagram of $MgFe_2O_4$ in three spinel forms, normal-spinel, mixed-spinel, and inverse-spinel, were studied using DFT in order to understand what the preferred surface terminations of $MgFe_2O_4$ are and why these orientations are stable, which is essential to determine the capture of Li^+ and the initial transport of Li^+ from surface to bulk. The low-index surfaces, $MgFe_2O_4$(1 0 0), (1 1 0), (1 1 1), and high-index surface of (3 1 1) were considered. These specific surfaces were chosen for consideration based on prior the high resolution transmission electron microscope (HR-TEM) results, showing that the bulk-terminated (2 2 0),[9] (1 1 1),[2c, 10] (2 2 2),[9b] (3 1 1),[9b, 11] (4 2 2)[12] and (5 1 1)[12] can be exposed facets of the $MgFe_2O_4$ crystal.

Further, the selected surface set for $MgFe_2O_4$ in this study is the same as that used previously for $ZnFe_2O_4$,[1] which allows close comparison between the two systems and thus enhances the fundamental insight into the effect of substituting Zn^{2+} for Mg^{2+} on the surface diagram of iron ferrite. In addition, consideration of three types of spinel structures for $MgFe_2O_4$ provides the opportunity to pinpoint the effect associated with the distribution of A^{2+} in the spinel structure. Indeed, our results rationalize the essential effect of the substitution of Zn^{2+} for Mg^{2+} in ferrite and provide new insights on how to control the shape of ferrite materials and thus tune the performances of LIBs.

2. Results and Discussion

2.1. $MgFe_2O_4$ Bulk and Surface

The supercell of $MgFe_2O_4$ bulk was constructed with the $Fd\bar{3}m$ primitive cell containing eight formula units in normal-spinel, mixed-spinel and inverse-spinel structures (Figure 1). According to the previous synchrotron X-ray powder diffraction (XPD) measurement,[13] for the mixed-spinel structure, 75% of the tetrahedral 8a sites were chosen to be occupied by Fe^{3+} ions and 25% of 8a sites are for Mg^{2+} ions, while 62.5% for Fe^{3+} ions and 37.5% for Mg^{2+} ions were considered in the case of the octahedral 16d sites. As summarized in Table 1, the DFT-optimized lattice parameters and band gaps of three systems are in reasonable agreement with the values measured experimentally[6b, 6h, 6j, 8b, 9a, 13].

Various possible bulk-terminations of $MgFe_2O_4$(1 0 0), $MgFe_2O_4$(1 1 0), $MgFe_2O_4$(1 1 1) and $MgFe_2O_4$(3 1 1) surfaces in normal-spinel, mixed-spinel and inverse-spinel structures were considered (Figure S1-S12), where each termination was labeled by the corresponding composition in our notation. Additionally, due to the lowered symmetry as compared to the normal-spinel, the $MgFe_2O_4$(0 0 1) and $MgFe_2O_4$(0 1 1) surfaces were also considered for the mixed-spinel and the inverse-spinel. The corresponding surface phase diagrams (Figure 2-4) were determined based on the calculated ζ as a function of $\Delta\mu_{Fe}$ and $\Delta\mu_O$ (see Experimental section for details).

Among the four surfaces studied for normal-spinel $MgFe_2O_4$, the (1 0 0) and (3 1 1) surfaces were found to be stable under a range of chemical potentials for which normal-spinel $MgFe_2O_4$ bulk is stable (Figure 2). Specifically, in the Fe-rich and O-rich region, the stoichiometric FeO_2-terminated $MgFe_2O_4$(1 0 0) or (1 0 0)-FeO_2 in our notation is more stable than the (1 0 0) with the Mg terminations or (1 0 0)-Mg, which becomes stable in the Mg-rich region. In the Fe-poor and O-rich region, the MgO_x-terminated $MgFe_2O_4$(3 1 1) surface, (3 1 1)-MgO_4, is preferred;

while at the Fe-intermediate region, the O-terminated $MgFe_2O_4$(3 1 1) surface, (3 1 1)-O^2, is favored. Yet, the preference for (3 1 1)-O^2 strongly depends on the chemical potential of O and Fe, which corresponds to a very small area in the surface phase diagram (Figure 2). In comparison, the other O-terminated $MgFe_2O_4$(3 1 1) surface, (3 1 1)-O^1, is the most likely surface configuration, which covers much larger area including most of the intermediate region. The difference between the two O-terminated surfaces is that the O^1-termination has a higher density of Mg^{2+} exposed to the surface (Figure 2), which is the descriptor to surface stability as demonstrated later. Our results indicate that the (3 1 1) is likely the dominant facet in normal-spinel $MgFe_2O_4$, which aligns with the previous experiments using XRD and TEM techniques. [9b, 11]

For the mixed-spinel $MgFe_2O_4$, the single orientation, {1 0 0} including (0 0 1) and (1 0 0), is favored under the condition that mixed-spinel $MgFe_2O_4$ bulk is stable (Figure 3). Specifically, the stoichiometric FeO_2-terminated $MgFe_2O_4$(0 0 1), (0 0 1)-FeO_2, is stable under both Fe-rich and O-rich condition, which is in alignment with case in normal-spinel (Figure 2), while the $MgFeO_x$-terminated $MgFe_2O_4$(1 0 0), (1 0 0)-$Mg_{1.5}Fe_{1.5}O_4$, is preferred at the Fe-rich and O-intermediate/poor region, rather than (3 1 1)-O^1 and (1 0 0)-Mg for the normal-spinel structure. The MgO_x-terminated $MgFe_2O_4$(0 0 1), (0 0 1)-MgO_4, rather than (3 1 1)-O^1 seen for the normal spinel structure, is the most likely surface configuration, which covers the relatively large area in the phase diagram including the Fe-poor and large intermediate region. In comparison, the mixed-spinel $MgFe_2O_4$(1 1 0), (0 1 1), (1 1 1) and (3 1 1) surfaces display higher cleavage energy ϑ (approximately 0.79 to 3.62 J/m^2), which measures the surface stability with respect to $MgFe_2O_4$ bulk, and metallic Mg and Fe (see Experimental section for detail) and do not appear in the surface phase diagram.

The inverse-spinel $MgFe_2O_4$, displays the most diverse distribution in facet orientation under a range of chemical potentials for which inverse-spinel $MgFe_2O_4$ bulk is stable, where the low-index surfaces (1 0 0), (0 0 1), (1 1 1) and high-index surface (3 1 1) can all be observed

(Figure 4). The Fe- and O-rich region is dominated by the stoichiometric O-terminated $MgFe_2O_4$(3 1 1), (3 1 1)-O, which is different from that in both normal-spinel and mixed-spinel structures. The (1 0 0)-$MgFeO_4$ and (0 0 1)-Mg_2FeO_4 surfaces are preferred at the Fe-intermediate or the O-intermediate region, similar to the mixed-spinel case. While the (1 1 1)-O surface covers the relatively large area in the phase diagram including the Fe-poor and extensive Fe- and O-intermediate regions. Given that, the (1 1 1) is likely the dominant facet in inverse-spinel $MgFe_2O_4$, which agrees well with the previous experiments using XRD, TEM and calculations on spinel LIB materials. [1, 2c, 7c, 9b, 10, 14]

According to the DFT calculations, the preferential facet orientation of $MgFe_2O_4$ crystal is sensitive to the distribution of Mg^{2+} in the spinel structure. The facet-preference shifts from (1 0 0) and (3 1 1) in the normal-spinel, solely {1 0 0} in the mixed-spinel, to (1 0 0), (0 0 1), (1 1 1) and (3 1 1) in the inverse-spinel (Figure 2-4). Accordingly, the equilibrium shape of $MgFe_2O_4$ crystal was estimated based on the Wulff's theorem[15]. The $MgFe_2O_4$ crystal is likely to adopt the truncated cubic shape surrounded with {1 0 0} and {3 1 1} (Figure 5a). While the perfect cube faceted by {1 0 0} is solely preferred for the mixed-spinel $MgFe_2O_4$ (Figure 5b). For the inverse-spinel $MgFe_2O_4$, the octahedral shape surrounded by eight {1 1 1} planes seems to dominate (Figure 5c); while only in the Fe/O-rich region, a rhombic triacontahedron with thirty {3 1 1} planes can be favored (Figure 5d), which is likely to account for the spherical particle observed in experiments[2b, 2c, 6b, 9b]. The DFT-predicted variation in crystal shape of $MgFe_2O_4$ with the distribution of Mg^{2+} ions well explains the observed variety of facets in previous HR-TEM, based on the samples synthesized under different conditions.[2c, 9-12]

2.2. Descriptor to Surface Stability of $MgFe_2O_4$

In our previous study on normal-spinel $ZnFe_2O_4$ surfaces, the low index surfaces of (1 1 0) with $ZnFeO_2$-termination, (1 1 1) with Zn-termination and O-termination are preferred in the

surface phase diagram.[1] It was found that the presence of stable FeO_6 octahedral layer parallel to the surface is responsible for the high stability of $ZnFe_2O_4$(1 1 1) (Figure S13). However, this does not seem to be the case for $MgFe_2O_4$. In this case, none of the above terminations are favored not only in normal-spinel $MgFe_2O_4$ by simply substituting Mg^{2+} for Zn^{2+}, but also in the mixed-spinel and the inverse-spinel $MgFe_2O_4$. That is the variation of A^{2+} in AFe_2O_4 from Zn to Mg changes the descriptor for the surface stability.

Our DFT calculations show that the descriptor to the surface stability is not associated with the FeO_6 octahedral layer, but the Mg^{2+} ions density exposed to the surface of $MgFe_2O_4$. The identification of Mg^{2+} ions density as the key descriptor is based on the statistics on densities of ions exposed for all the surfaces studied. Among all the ions in $MgFe_2O_4$, a clear linear relationship between the density of Mg^{2+} and the cleavage energy ϑ is observed (Figure 6), where the lower density of Mg^{2+} corresponds to the higher ϑ or the lower surface stability. While no clear correlation is observed between the surface stability and the densities of both Fe^{3+} and O^{2-} ions (Figure S14).

To understand the capability of Mg^{2+} in the stabilization of $MgFe_2O_4$ surfaces, the projected density of states (PDOS) of surface Fe^{3+}, Mg^{2+} and O^{2-} in $MgFe_2O_4$ was plotted (Figure 7). Common features in PDOS were observed despite of the diversity in surface diagram for normal (Figure 7a), mixed (Figure 7b) and inverse spinel (Figure 7c) structures. Firstly, the conduction bands in $MgFe_2O_4$ are dominated by Fe 3d states and the valences bands are composed of Fe 3d states and O 2s2p states, as seen for the case of $ZnFe_2O_4$.[1] The difference emerges for the A^{2+} ions. In $ZnFe_2O_4$,[1] Zn 3d states dominate the states at ~ -5 eV below the Fermi level; while little contribution from Mg is observed. That is, when exposed to the surface, Mg is still in the oxidized divalent states due to the strong Mg-O binding. Mg^{2+} ions are more stable than Zn^{2+}, Fe^{3+} and O^{2-} ions on the surface. Due to the extremely high stability of Mg^{2+}, the surface stability of $MgFe_2O_4$ is more dependent on the density of Mg^{2+} ions than the other ions as shown in Figure 6. In addition, such strong dependence on density of exposed Mg^{2+} ions likely

overwhelm the contribution from the FeO_6 octahedral layer parallel to the surface, which explains well the divergence of the surface phase diagram induced by substitution of Zn^{2+} for Mg^{2+}, even though the same normal-spinel structure is adopted (Figures 2 and S13). We note that the tuning principle of A^{2+} extracted above can vary from one case to the next. According to the present results, there are significant changes in structures of bulk and surfaces of AFe_2O_4 when moving from A = Zn to A = Mg. though both Zn^{2+} and Mg^{2+} ions are is relatively stable. While more variations are likely observed by using less stable A^{2+}, e.g. Cu^{2+}, Mn^{2+}, Co^{2+}, where the situation can be more complicated and detailed investigation is necessary.

3. Conclusion

We employed DFT to study the surface structures and stability of the low-index surfaces, $MgFe_2O_4$(1 0 0), (1 1 0), (1 1 1), and high-index surface of (3 1 1). The consideration of three types of spinel conformations, normal-spinel, mixed-spinel and inverse-spinel structures and the close comparison with $ZnFe_2O_4$ enable the gain of fundamental understanding on tuning capability of distribution and intrinsic property of A^{2+} ion toward the structures of spinel AFe_2O_4.

The variation in the distribution of Mg^{2+} ion within the spinel structure offers the shape-tuning of $MgFe_2O_4$ crystal. The normal-spinel $MgFe_2O_4$ favors (1 0 0) and (3 1 1) surface orientation under a range of chemical potentials for which the corresponding bulk is stable, leading to a truncated cubic morphology. In the case of mixed-spinel $MgFe_2O_4$, only the low-index surface (1 0 0) and (0 0 1) surfaces are stable, which likely favors the formation of a cubic particle; while the (1 0 0), (0 0 1), (1 1 1) and (3 1 1) surface are all preferred for the inverse-spinel $MgFe_2O_4$, and the octahedral shape can be the dominant. The variation of A^{2+} ion from Zn^{2+} to Mg^{2+} changes the descriptors to the surface stability, going from the presence of the

FeO_6 octahedral layer parallel to the surface to the density of highly stable Mg^{2+} ion exposed to the surface. Our results not only explain well the experimental observations on diverse morphologies of $MgFe_2O_4$, but also provide the guidance to tune the structures and likely the LIB behaviors of ferrite by substituting Zn^{2+} for Mg^{2+}, which is difficult to achieve experimentally, but key to the rational design of spinel materials as LIBs materials.

4. Experimental Section

DFT Calculations: DFT implemented in the Vienna ab initio simulation package (VASP)[16] was employed. The spin-polarized DFT+U calculations[17] were carried out with the PAW potential[16b, 18] using the PBE exchange-correlation functional[19] and a kinetic energy cutoff of 520 eV. A Hubbard U correction of U_{eff} = 5.3 eV was applied to the Fe d orbitals. This setup was successfully used to predict the structures and properties for other spinel systems according to our previous studies.[1, 2d, 3, 7b] The Gaussian smearing method was used with the total energies converged better than 10^{-5} eV, and the final force on each atom is less than 0.02 eV $Å^{-1}$. The first Brillouin zone was sampled on 3 × 3 × 1 k-mesh.

Surface Stability Calculations: The slab model was considered to describe various $MgFe_2O_4$ surfaces. The surface was modeled using a 2 × 2 surface slab. To eliminate the effect introduced by different terminations on both ends of a slab surface, the same terminations were chosen. The number of layers included varied depending on the termination, making sure that the slab was terminated by the same surface termination. A 20 Å thick vacuum was added along the direction perpendicular to the surface to avoid the artificial interactions between the slabs. During geometry optimization, the top and bottom three layers were allowed to relax, while the rest were fixed at the bulk positions.

Following the previous studies[1, 7a, 20], the stability of surface was determined by the surface energy defined as

$$\zeta = \frac{E_{Slab} - x\mu_{Mg} - y\mu_{Fe} - z\mu_O}{2S} \quad (1)$$

where E_{slab} is the total energy of $Mg_xFe_yO_z$ surfaces. μ_{Mg}, μ_{Fe}, μ_O are the chemical potential of Mg, Fe, O, respectively, in $Mg_xFe_yO_z$ surfaces; S is the surface area of the slab.

The μ_{Mg}, μ_{Fe} and μ_O has a range in which $MgFe_2O_4$ bulk is stable,

$$\mu_{MgFe2O4} = \mu_{Mg} + 2\mu_{Fe} + 4\mu_O = E_{MgFe2O4} \quad (2)$$

$$\Delta\mu_{Mg} = \mu_{Mg} - E_{Mg} < 0 \quad (3)$$

$$\Delta\mu_{Fe} = \mu_{Fe} - E_{Fe} < 0 \quad (4)$$

$$\Delta\mu_O = \mu_O - E_O < 0 \quad (5)$$

where E_{Mg}, E_{Fe}, E_O are the total energy of metallic Mg bulk, metallic Fe bulk, and O in gaseous molecular O_2, respectively; $\Delta\mu_{Mg}$, $\Delta\mu_{Fe}$ and $\Delta\mu_O$ refer to the difference of chemical potential in the slab and in metallic bulk (Mg and Fe) or gas phase (O), at 0 K and 1 bar. Therefore, a more negative value indicates a Fe or O poor condition; while a value closes to 0 represents a Fe or O rich environment condition. This method has been proven previously, being able to describe well the experimental results of spinel metal oxide surfaces including Fe_3O_4,[7a] $ZnFe_2O_4$[1] and $LiMn_2O_4$[20c, 20d].

Therefore, the surface energy was expressed as a function of $\Delta\mu_{Fe}$ and $\Delta\mu_O$

$$\zeta = \vartheta - \frac{\left(\frac{y}{2} - x\right)\Delta\mu_{Fe} + \left(\frac{z}{4} - x\right)\Delta\mu_O}{2S} \quad (6)$$

$$\vartheta = \frac{E_{slab} - xE_{ZnFe_2O_4} - \left(\frac{y}{2} - x\right)E_{Fe} - \left(\frac{z}{4} - x\right)E_O}{2S} \quad (7)$$

where ϑ is the cleavage energy, a constant that measures the surface stability with respect to $MgFe_2O_4$ bulk, and metallic Mg, Fe. Based on the equations, the phase diagrams of various surfaces with different terminations of $MgFe_2O_4$ were determined.

Supporting Information

Supporting Information is available from the Wiley Online Library or from the author.

Acknowledgements

This work was carried out at Brookhaven National Laboratory (BNL), and was funded as part of the Center for Mesoscale Transport Properties (m2M), an Energy Frontier Research Center (EFRC) supported by the U.S. Department of Energy, Office of Science, Basic Energy Sciences, under Award No. DE-SC0012673. MRCAT operations are supported by the Department of Energy and the MRCAT member institutions. The DFT calculations were performed using computational resources at the Center for Functional Nanomaterials, which is a U.S. DOE Office of Science Facility, and the Scientific Data and Computing Center, a component of the BNL Computational Science Initiative, at BNL.

References

[1] H. Guo, A. C. Marschilok, K. J. Takeuchi, E. S. Takeuchi, P. Liu, *ACS Appl. Mater. Interfaces* **2018**, 10, 35623−35630.

[2] a) N. Sivakumar, S. R. P. Gnanakan, K. Karthikeyan, S. Amaresh, W. S. Yoon, G. J. Park, Y. S. Lee, *J. Alloys Compd.* **2011**, 509, 7038; b) C. Gong, Y.-J. Bai, Y.-X. Qi, N. Lun, J. Feng, *Electrochim. Acta* **2013**, 90, 119; c) Y. Pan, Y. Zhang, X. Wei, C. Yuan, J. Yin, D. Cao, G. Wang, *Electrochim. Acta* **2013**, 109, 89; d) Y. Zhang, C. J. Pelliccione, A. B. Brady, H. Guo, P. F. Smith, P. Liu, A. C. Marschilok, K. J. Takeuchi, E. S. Takeuchi, *Chem. Mater.* **2017**, 29, 4282.

[3] H. Guo, Y. Zhang, A. C. Marschilok, K. J. Takeuchi, E. S. Takeuchi, P. Liu, *Phys. Chem. Chem. Phys.* **2017**, 19, 26322.

[4] Z. Ma, Y. Wang, C. Sun, J. A. Alonso, M. T. Fernandez-Diaz, L. Chen, *Scientific Reports* **2014**, 4, 7231.

[5] Y. Gong, W. Ding, Z. Li, R. Su, X. Zhang, J. Wang, J. Zhou, Z. Wang, Y. Gao, S. Li, P. Guan, Z. Wei, C. Sun, *ACS Catal.* **2018**, 8, 4082.

[6] a) Q. Chen, A. J. Rondinone, B. C. Chakoumakos, Z. J. Zhang, *J. Magn. Magn. Mater.* **1999**, 194, 1; b) C. Liu, B. Zou, A. J. Rondinone, Z. J. Zhang, *J. Am. Chem. Soc.* **2000**, 122, 6263; c) V. Šepelák, D. Baabe, F. J. Litterst, K. D. Becker, *J. Appl. Phys.* **2000**, 88, 5884; d) M. Gateshki, V. Petkov, S. K. Pradhan, T. Vogt, *J. Appl. Cryst.* **2005**, 38, 772; e) P. Holec, J. Plocek, D. Nižňanský, J. Poltierová Vejpravová, *J. Sol-Gel Sci. Technol.* **2009**, 51, 301; f) N. Sivakumar, A. Narayanasamy, J. M. Greneche, R. Murugaraj, Y. S. Lee, *J. Alloys Compd.* **2010**, 504, 395; g) S. Da Dalt, A. S. Takimi, T. M. Volkmer, V. C. Sousa, C. P. Bergmann, *Powder Technol.* **2011**, 210, 103; h) S. Permien, S. Indris, M. Scheuermann, U. Schürmann, V. Mereacre, A. K. Powell, L. Kienle, W. Bensch, *J. Mater. Chem. A* **2015**, 3, 1549; i) B. Zheng, S. Wu, X. Yang, M. Jia, W. Zhang, G. Liu, *ACS Appl. Mater. Interfaces* **2016**, 8, 26683; j) J. Guo, L. Shi, L. Wu, S. Pan, X. Yuan, J. Zhao, *Mater. Res. Express* **2018**, 5.

[7] a) R. Pentcheva, F. Wendler, H. L. Meyerheim, W. Moritz, N. Jedrecy, M. Scheffler, *Phys. Rev. Lett.* **2005**, 94, 126101; b) W. Zhang, D. C. Bock, C. J. Pelliccione, Y. Li,

L. Wu, Y. Zhu, A. C. Marschilok, E. S. Takeuchi, K. J. Takeuchi, F. Wang, *Adv. Energy Mater.* **2016**, 6, 1502471; c) Y. Song, W. Mi, X. Wang, *Adv. Mater. Interfaces* **2016**, 3; d) L. Wang, Y. Zhang, H. Guo, J. Li, E. A. Stach, X. Tong, E. S. Takeuchi, K. J. Takeuchi, P. Liu, A. C. Marschilok, S. S. Wong, *Chem. Mater.* **2018**, 30, 671; e) Y. Chen, L. Ben, B. Chen, W. Zhao, X. Huang, *Adv. Mater. Interfaces* **2018**, 5; f) F. Liu, D. Y. Xie, M. Bugnet, T. Majdi, J. S. Preston, J. Wang, G.-z. Zhu, *Adv. Mater. Interfaces* **2018**, 5.

[8] a) D. M. Wells, J. Cheng, D. E. Ellis, B. W. Wessels, *Phys. Rev. B* **2010**, 81; b) R. Dom, R. Subasri, K. Radha, P. H. Borse, *Solid State Commun.* **2011**, 151, 470; c) V. Nagarajan, A. Thayumanavan, R. Chandiramouli, *Processing and Application of Ceramics* **2017**, 11, 296; d) L. Sharma, R. Kakkar, *J. Environ. Chem. Eng.* **2018**, 6, 6891.

[9] a) Y. Hou, F. Zuo, A. Dagg, P. Feng, *Angew. Chem. Int. Ed.* **2013**, 52, 1248; b) A. K. Rai, T. V. Thi, J. Gim, J. Kim, *Mater. Charact.* **2014**, 95, 259; c) Y. Liu, P. Zhang, M. Fan, P. Jiang, *Fuel* **2016**, 164, 314.

[10] Y. Guo, G. Qin, E. Liang, M. Li, C. Wang, *Ceram. Int.* **2017**, 43, 12519.

[11] a) V. K. Tripathi, R. Nagarajan, *Adv. Powder Technol.* **2016**, 27, 1251; b) Y. Zu, Y. Zhao, K. Xu, Y. Tong, F. Zhao, *Ceram. Int.* **2016**, 42, 18844.

[12] Y. Guo, Y. Zhu, C. Yuan, C. Wang, *Mater. Lett.* **2017**, 199, 101.

[13] D. Bock, K. Tallman, H. Guo, P. Smith, M. Huie, B. Zhang, D. Lutz, A. McCarthy, V. Burnett, A. Bruck, A. C. Marschilok, E. S. Takeuchi, P. Liu, K. J. Takeuchi, *Chem. Mater.* **2019**, Submitted.

[14] K. L. Bassett, R. E. Warburton, S. Deshpande, T. T. Fister, K. Ta, J. L. Esbenshade, A. Kinaci, M. K. Y. Chan, K. M. Wiaderek, K. W. Chapman, J. P. Greeley, A. A. Gewirth, *Adv. Mater. Interfaces* **2019**, 6.

[15] a) W. Kaminsky, *J. Appl. Cryst.* **2005**, 38, 566; b) W. Kaminsky, *J. Appl. Cryst.* **2007**, 40, 382.

[16] a) G. Kresse, J. Furthmüller, *Phys. Rev. B* **1996**, 54, 11169; b) G. Kresse, D. Joubert, *Phys. Rev. B* **1999**, 59, 1758.

[17] a) V. I. Anisimov, J. Zaanen, O. K. Andersen, *Phys. Rev. B* **1991**, 44, 943; b) V. I. Anisimov, F. Aryasetiawan, A. I. Lichtenstein, *J. Phys. Condens. Matter* **1997**, 9, 767.

[18] P. E. Blöchl, *Phys. Rev. B* **1994**, 50, 17953.

[19] J. P. Perdew, K. Burke, M. Ernzerhof, *Phys. Rev. Lett.* **1996**, 77, 3865.

[20] a) G.-X. Qian, R. M. Martin, D. J. Chadi, *Phys. Rev. B* **1988**, 38, 7649; b) M. Wagner, S. Seiler, B. Meyer, L. A. Boatner, M. Schmid, U. Diebold, *Adv. Mater. Interfaces* **2014**, 1; c) S. Kim, M. Aykol, C. Wolverton, *Phys. Rev. B* **2015**, 92, 115411; d) R. E. Warburton, H. Iddir, L. A. Curtiss, J. P. Greeley, *ACS Appl. Mater. Interfaces* **2016**, 8, 11108.

Figures and Captions

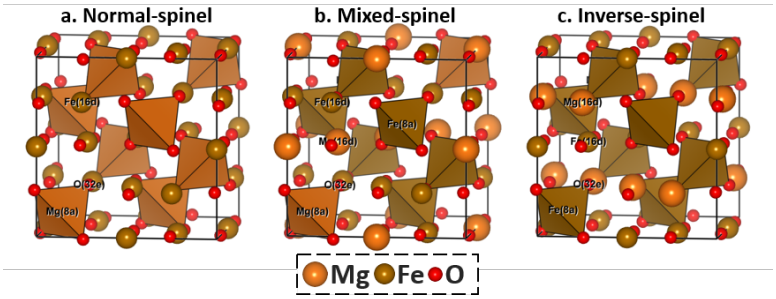

Figure 1. Structures of normal-spinel (a), mixed-spinel (b), inverse-spinel (c) $MgFe_2O_4$.

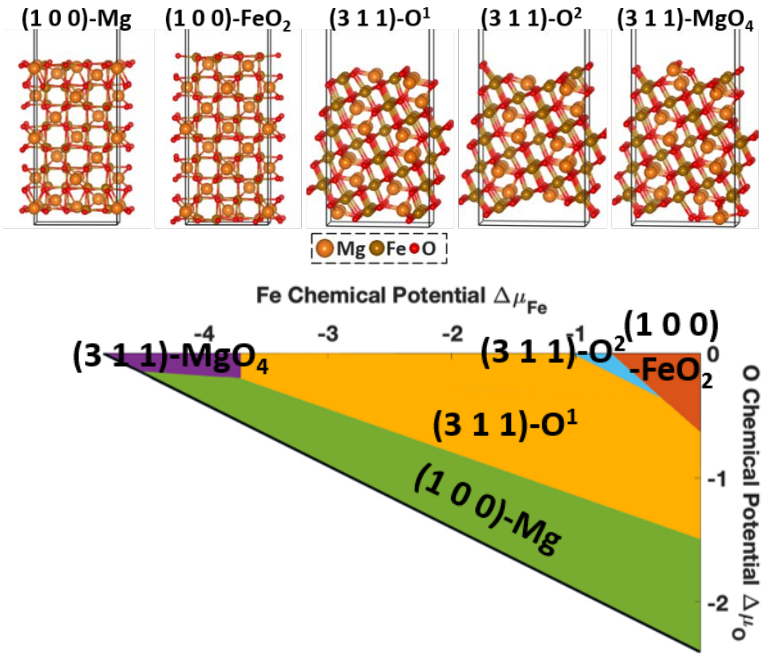

Figure 2. Surface phase diagram and the corresponding structures of normal-spinel $MgFe_2O_4$.

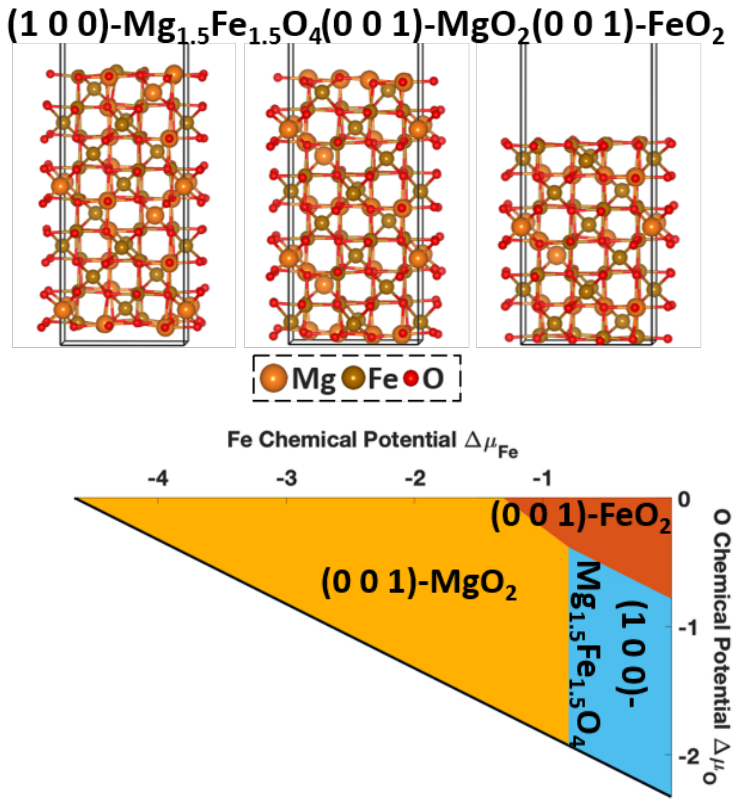

Figure 3. Surface phase diagram and the corresponding structures of mixed-spinel $MgFe_2O_4$.

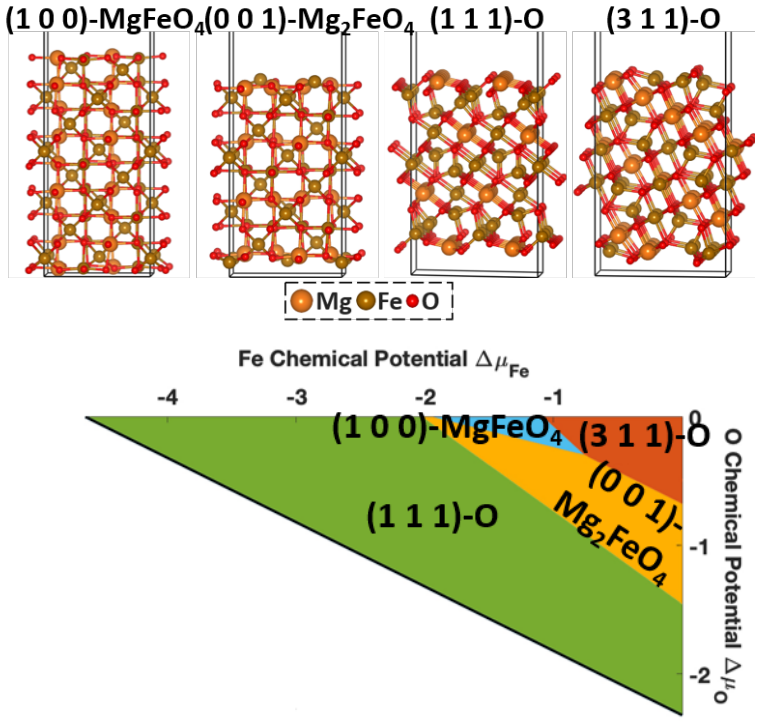

Figure 4. Surface phase diagram and the corresponding structures of inverse-spinel $MgFe_2O_4$.

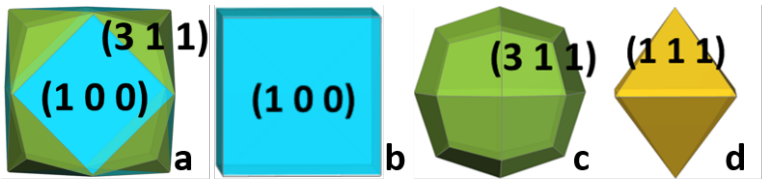

Figure 5. Schematic morphology of $MgFe_2O_4$ crystal including truncated cubic (a), cubic (b), octahedral (c) and rhombic (d) shapes.

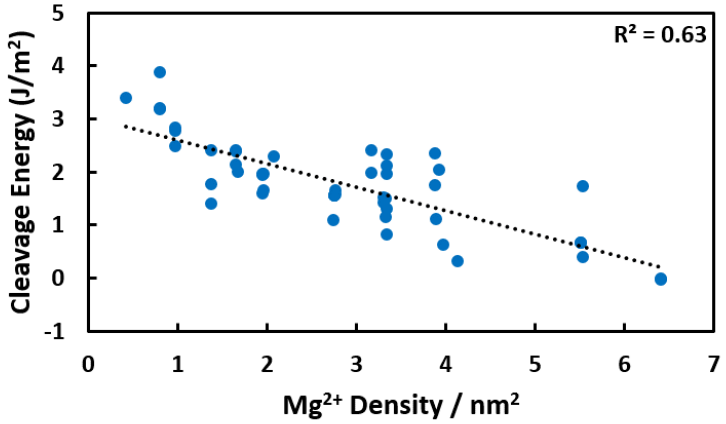

Figure 6. Correlation between the cleave energy (J/m^2) and Mg^{2+} density per nm^2 exposed to the surface.

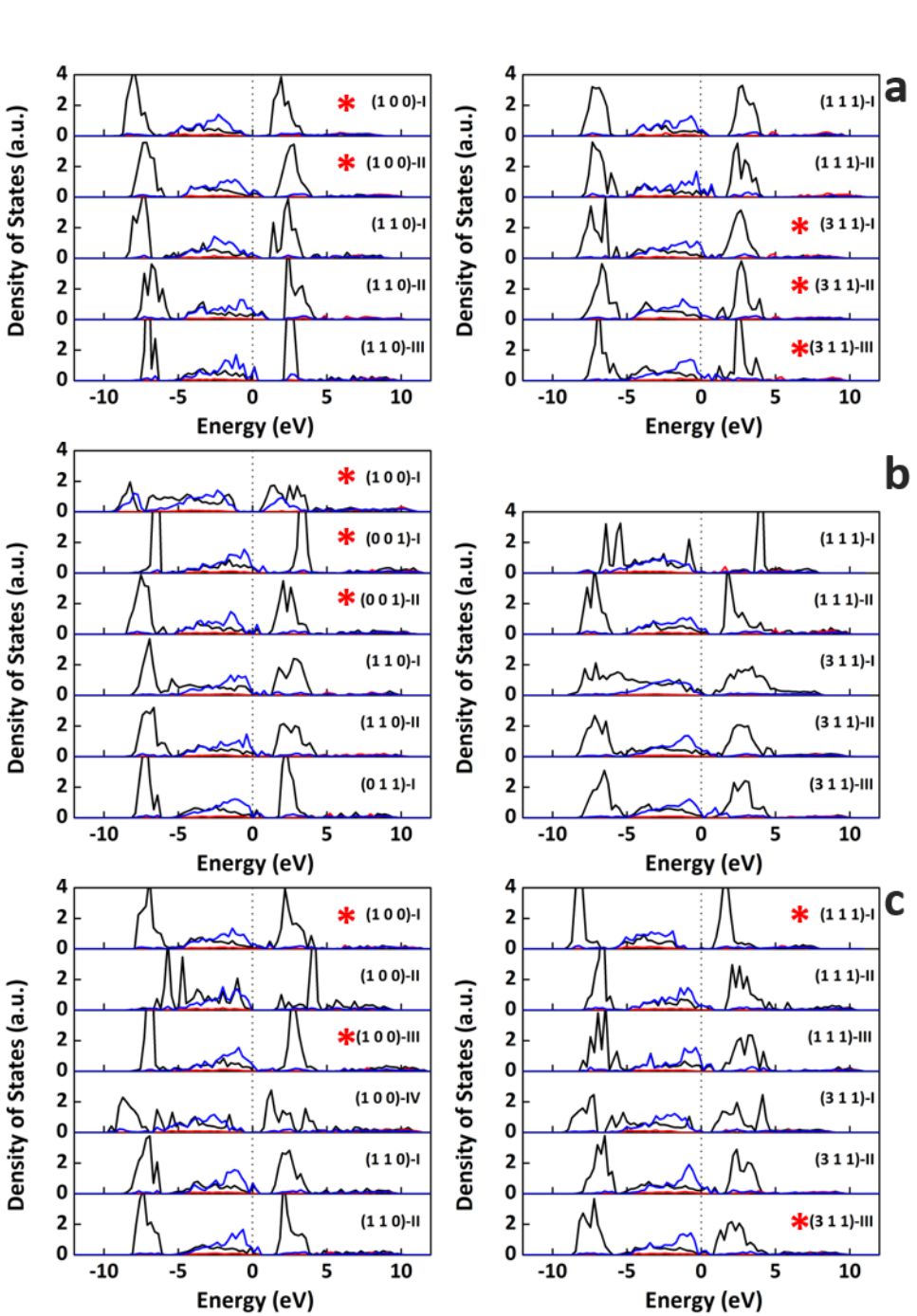

Figure 7. Projected density of states (PDOS) of surface Mg^{2+}(red), Fe^{3+}(black) and O^{2-}(blue) in normal-spinel (a), mixed-spinel (b) and inverse-spinel (c) $MgFe_2O_4$. The stable facets in the phase diagram are marked with star.

Table 1. The lattice parameters and band gaps of normal-spinel, mixed-spinel and inverse-spinel $MgFe_2O_4$, in comparison with experimental data.

	Normal-spinel	Mixed-spinel	Inverse-spinel	Experiment
Lattice parameter a = b = c (Å)	8.54	8.52	8.50	8.40[6b], 8.39[6h], 8.38[13]
Band gap (eV)	1.5	1.5	1.5	2.0[9a] 1.9[8b] 1.6[6j]

Table of Contents

The diverse surface structures and stability of $MgFe_2O_4$, a perspective anode material for lithium ion battery, are extensively studied using density functional theory. The preferential facet orientation of $MgFe_2O_4$ crystal is found to be sensitive to the distribution of Mg^{2+} in the spinel structure. However, there is one common descriptor to all the stable surfaces among all three $MgFe_2O_4$ systems: high density of Mg^{2+} exposed to the surface.

Keyword $MgFe_2O_4$, ferrite, spinel, DFT, surface diagram

Haoyue Guo, Amy C. Marschilok, Kenneth J. Takeuchi, Esther S. Takeuchi, Ping Liu*

Rationalization of Diversity in Spinel $MgFe_2O_4$ Surfaces

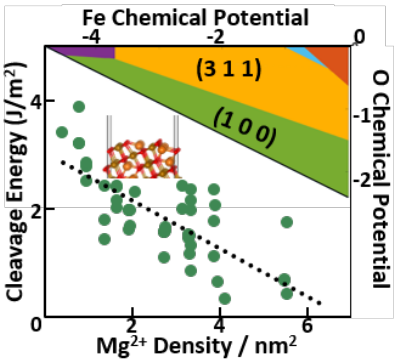

Supporting Information

Rationalization of Diversity in Spinel $MgFe_2O_4$ Surfaces

*Haoyue Guo, Amy C. Marschilok, Kenneth J. Takeuchi, Esther S. Takeuchi, and Ping Liu**

Results

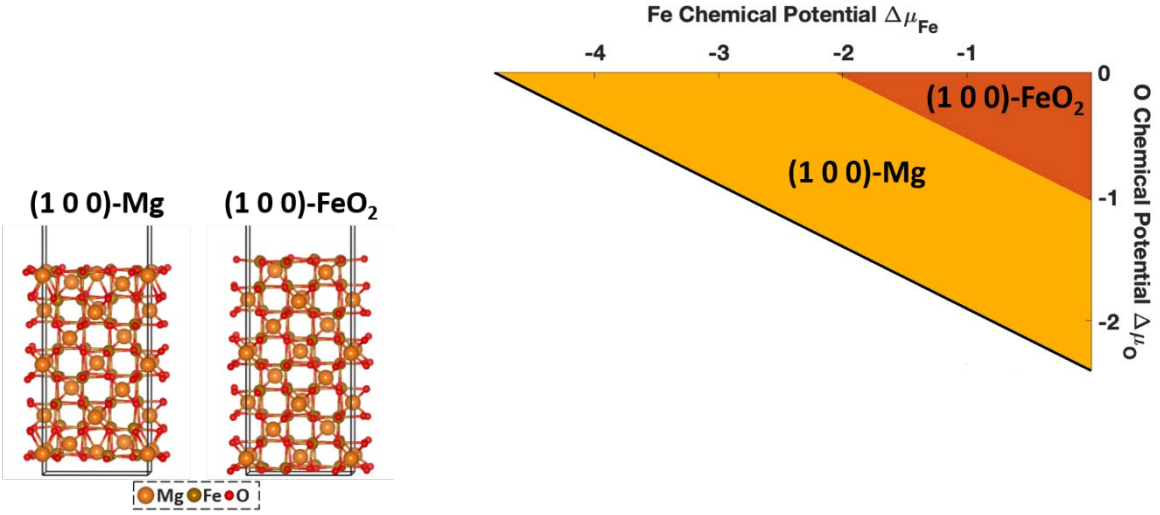

Figure S1. Surface phase diagram and structures of normal-spinel $MgFe_2O_4$(1 0 0). Low energy surface terminations are shown for $MgFe_2O_4$ (1 0 0) in $\Delta\mu_{Fe}$ and $\Delta\mu_O$ phase space.

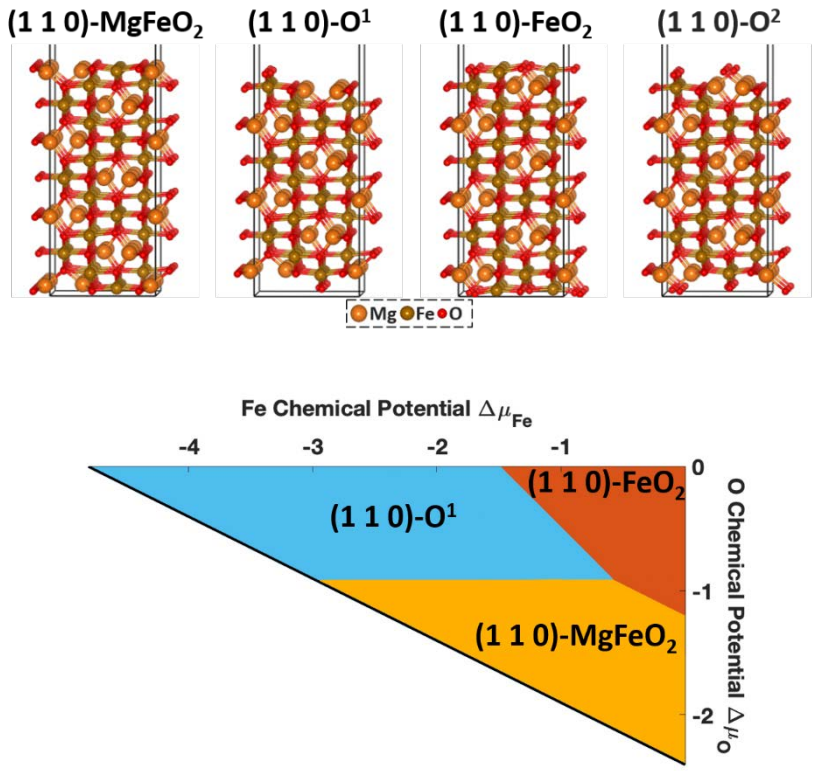

Figure S2. Surface phase diagram and structures of normal-spinel $MgFe_2O_4$(1 1 0). Low energy surface terminations are shown for $MgFe_2O_4$ (1 1 0) in $\Delta\mu_{Fe}$ and $\Delta\mu_O$ phase space.

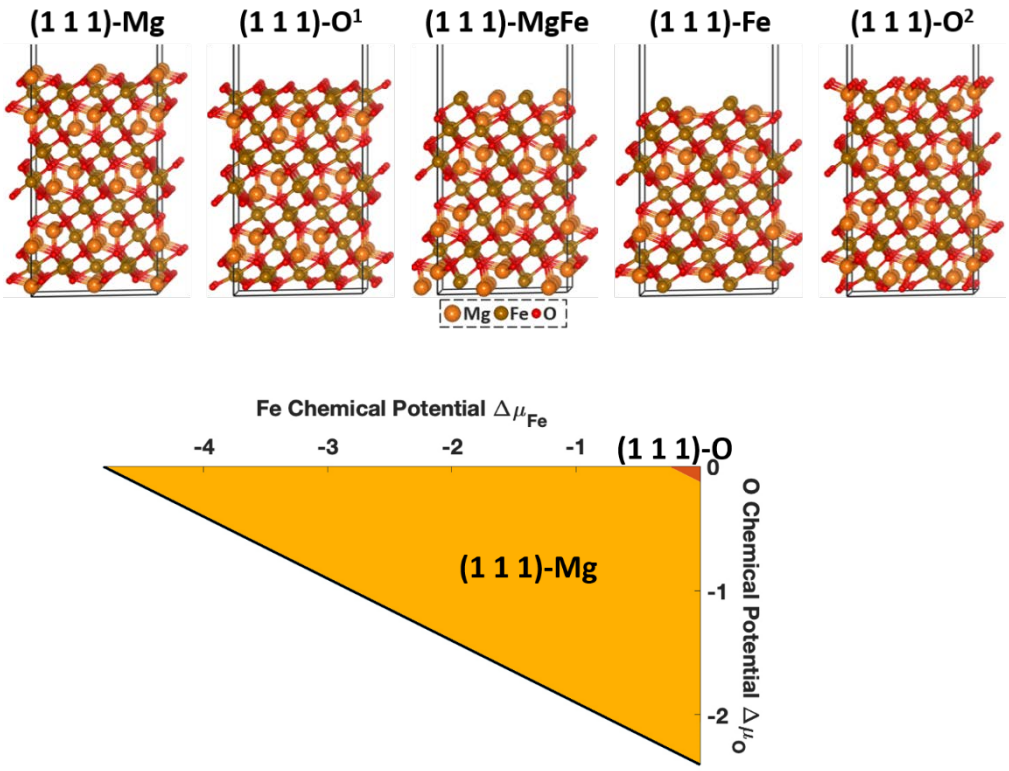

Figure S3. Surface phase diagram and structures of normal-spinel $MgFe_2O_4$(1 1 1). Low energy surface terminations are shown for $MgFe_2O_4$ (1 1 1) in $\Delta\mu_{Fe}$ and $\Delta\mu_O$ phase space.

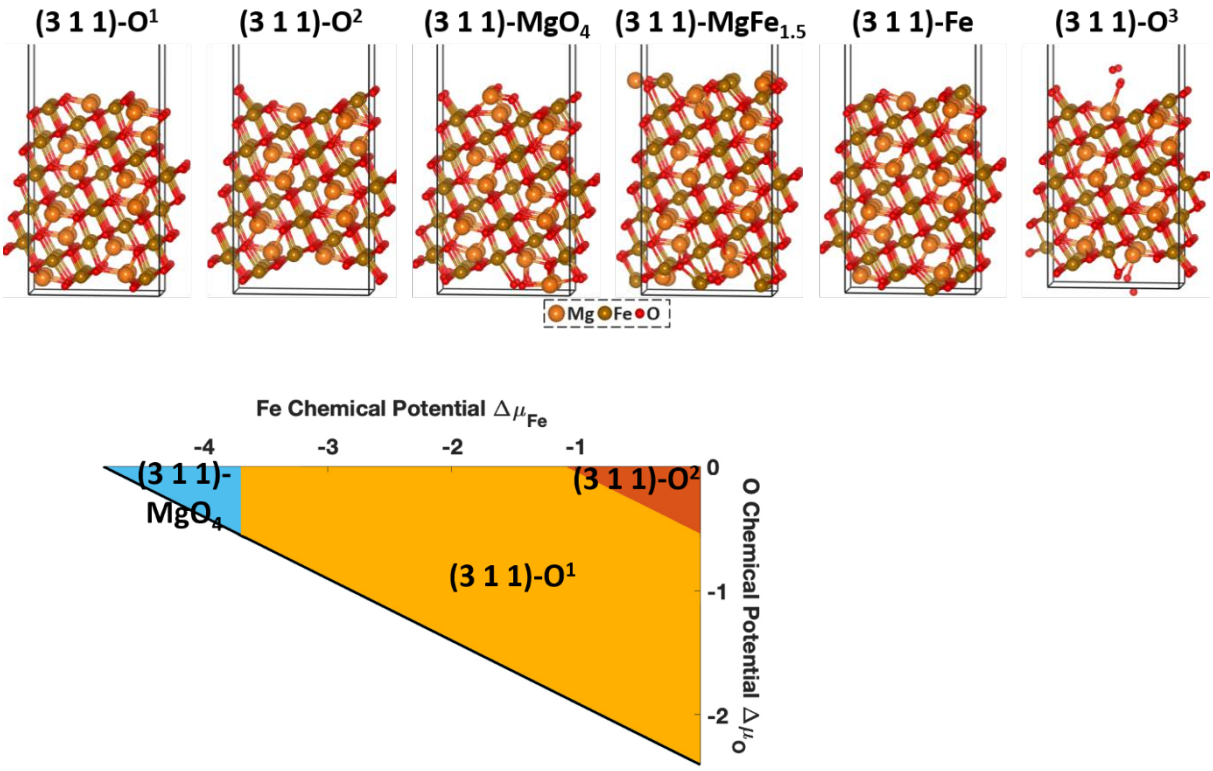

Figure S4. Surface phase diagram and structures of normal-spinel $MgFe_2O_4$(3 1 1). Low energy surface terminations are shown for $MgFe_2O_4$ (3 1 1) in $\Delta\mu_{Fe}$ and $\Delta\mu_O$ phase space.

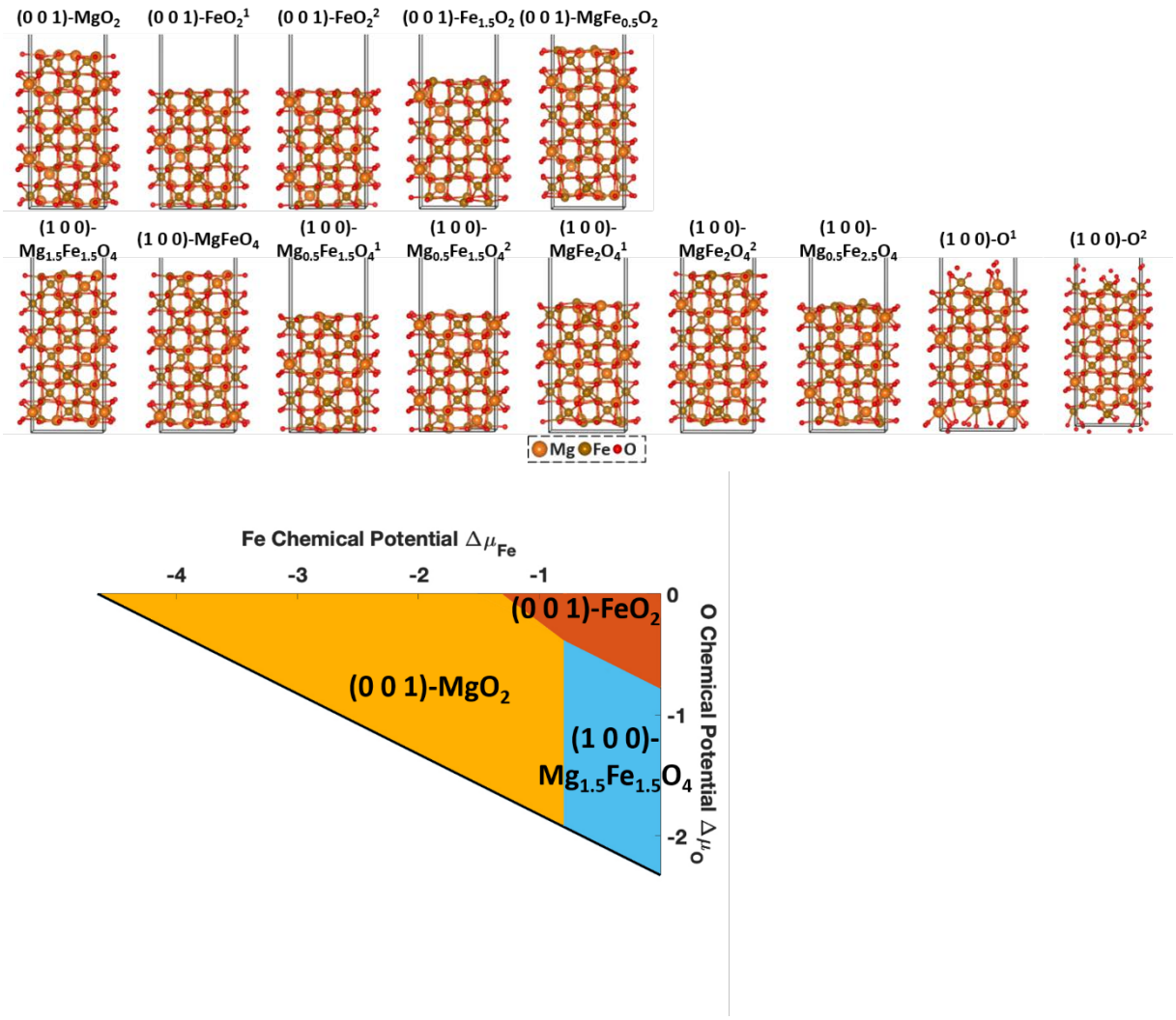

Figure S5. Surface phase diagram and structures of mixed-spinel $MgFe_2O_4$(1 0 0) and (0 0 1). Low energy surface terminations are shown for $MgFe_2O_4$ (1 0 0) and (0 0 1) in $\Delta\mu_{Fe}$ and $\Delta\mu_O$ phase space.

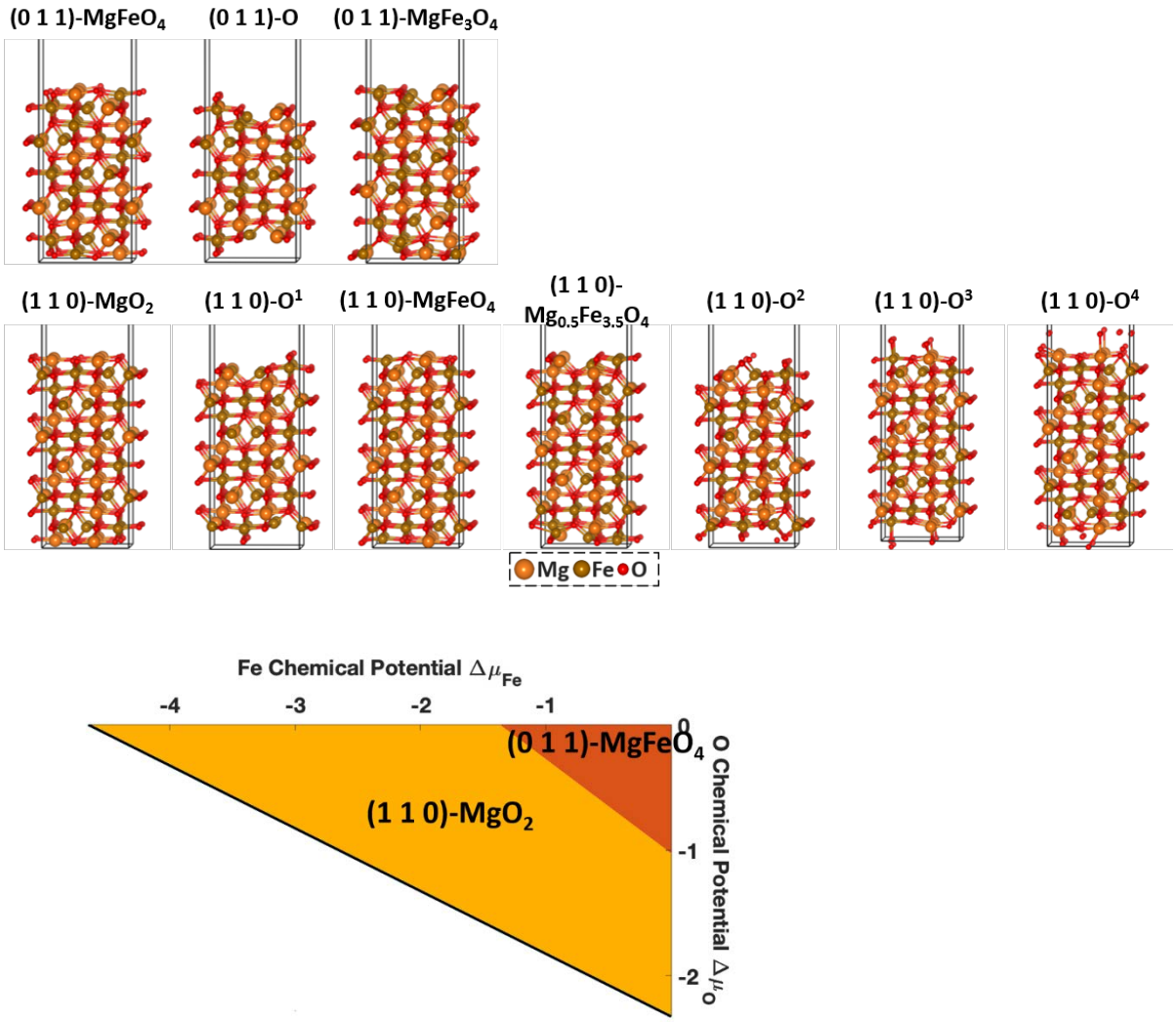

Figure S6. Surface phase diagram and structures of mixed-spinel $MgFe_2O_4$(1 1 0) and (0 1 1). Low energy surface terminations are shown for $MgFe_2O_4$ (1 1 0) and (0 1 1) in $\Delta\mu_{Fe}$ and $\Delta\mu_O$ phase space.

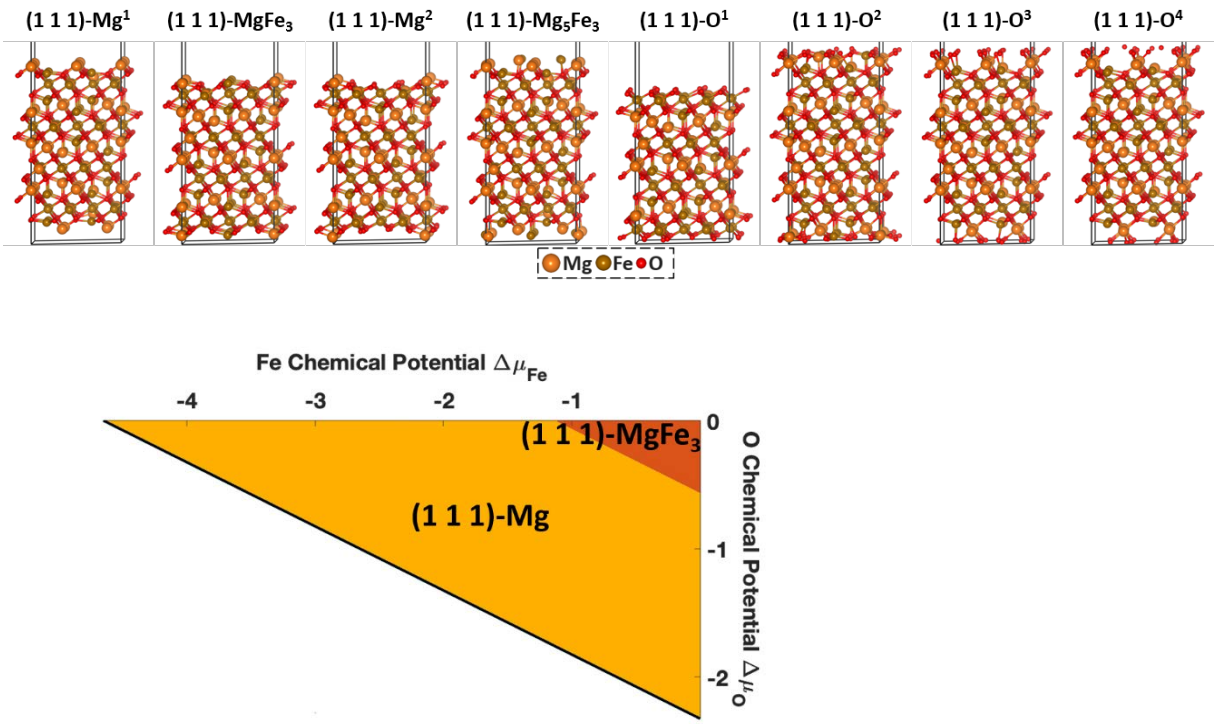

Figure S7. Surface phase diagram and structures of mixed-spinel $MgFe_2O_4$(1 1 1). Low energy surface terminations are shown for $MgFe_2O_4$ (1 1 1) in $\Delta\mu_{Fe}$ and $\Delta\mu_O$ phase space.

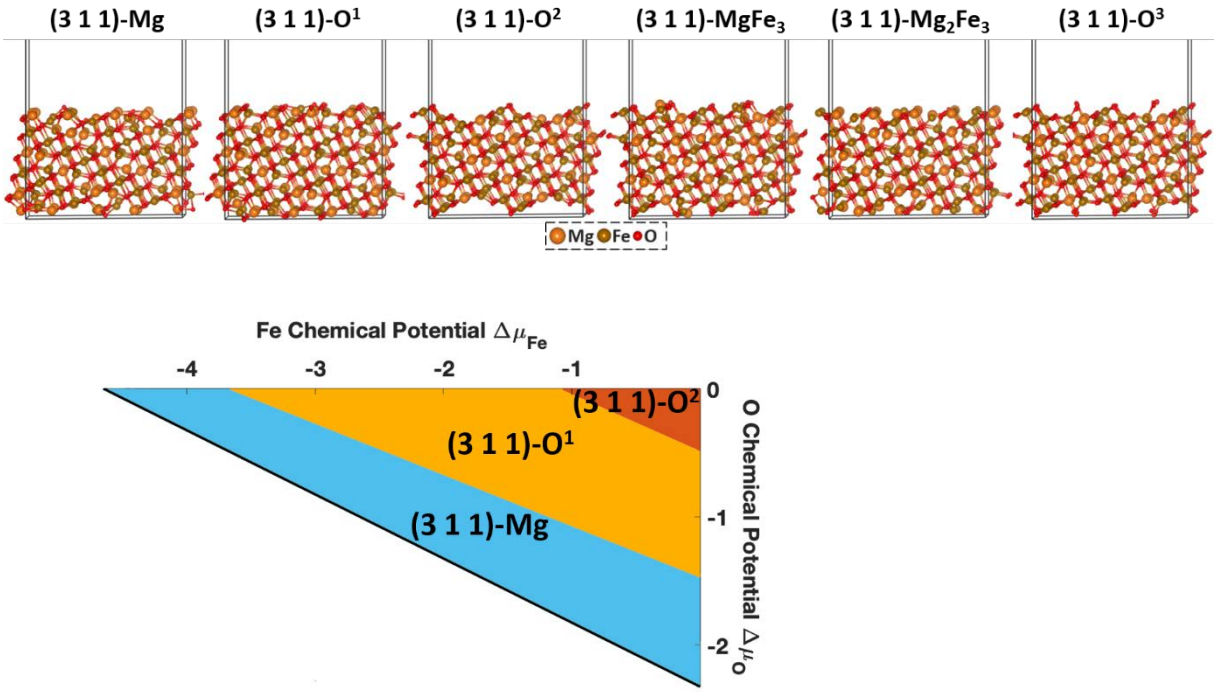

Figure S8. Surface phase diagram and structures of mixed-spinel $MgFe_2O_4$(3 1 1). Low energy surface terminations are shown for $MgFe_2O_4$ (3 1 1) in $\Delta\mu_{Fe}$ and $\Delta\mu_O$ phase space.

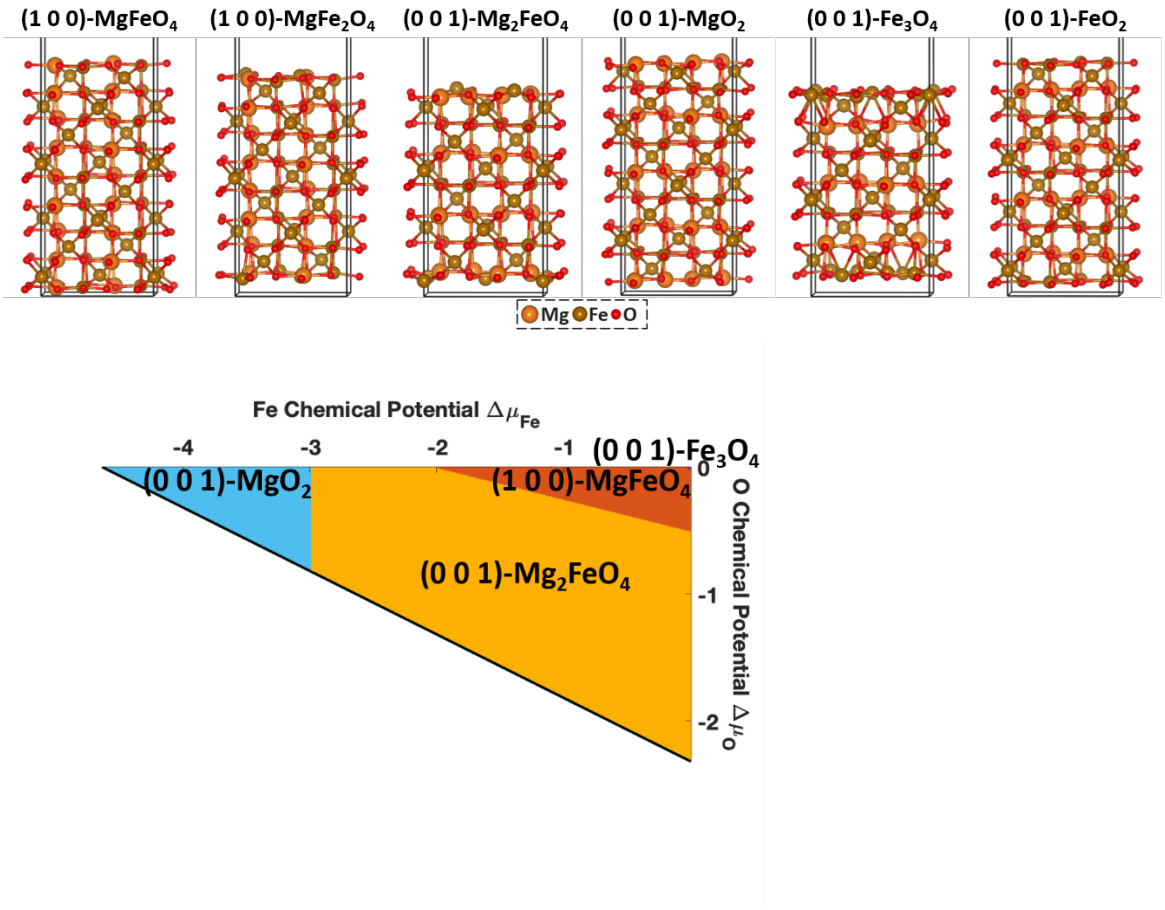

Figure S9. Surface phase diagram and structures of inverse-spinel $MgFe_2O_4$(1 0 0) and (0 0 1). Low energy surface terminations are shown for $MgFe_2O_4$ (1 0 0) and (0 0 1) in $\Delta\mu_{Fe}$ and $\Delta\mu_O$ phase space.

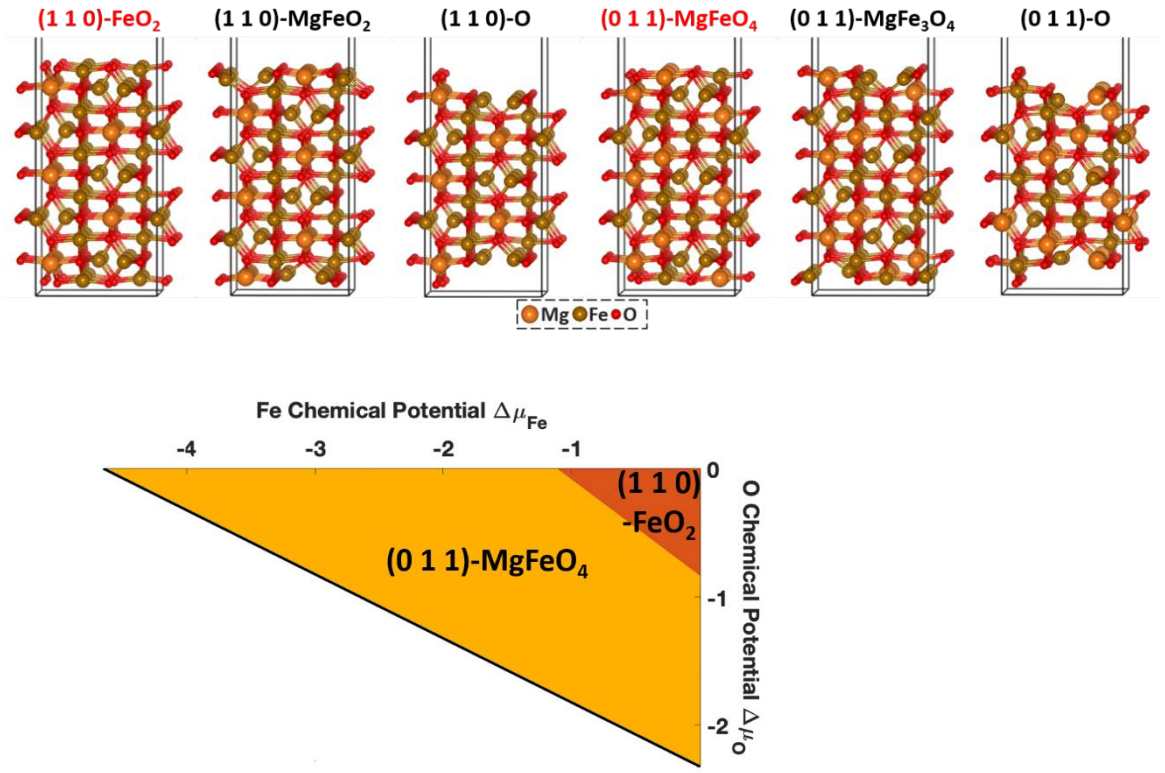

Figure S10. Surface phase diagram and structures of inverse-spinel $MgFe_2O_4$(1 1 0) and (0 1 1). Low energy surface terminations are shown for $MgFe_2O_4$ (1 1 0) and (0 1 1) in $\Delta\mu_{Fe}$ and $\Delta\mu_O$ phase space.

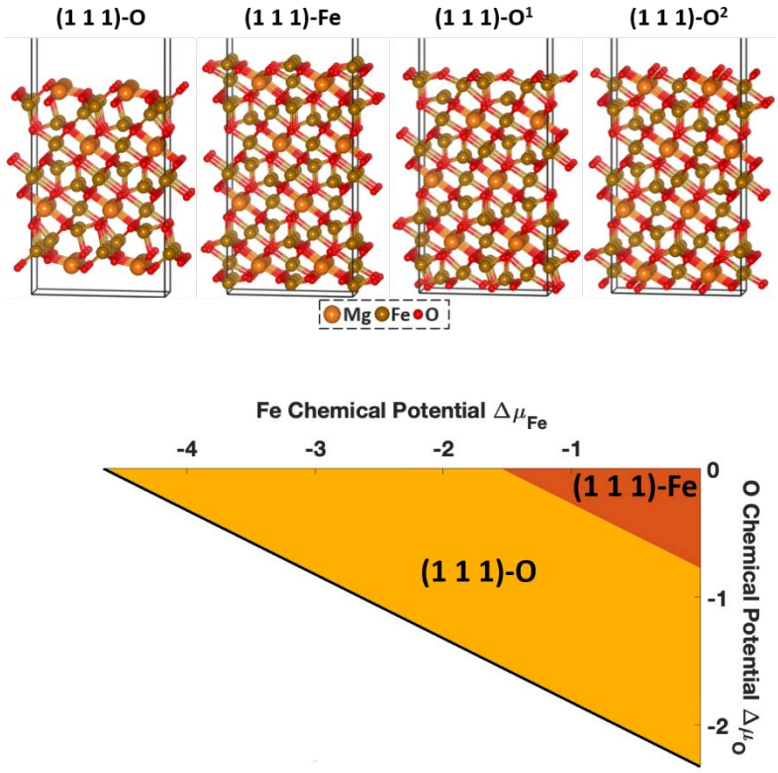

Figure S11. Surface phase diagram and structures of inverse-spinel $MgFe_2O_4$(1 1 1). Low energy surface terminations are shown for $MgFe_2O_4$ (1 1 1) in $\Delta\mu_{Fe}$ and $\Delta\mu_O$ phase space.

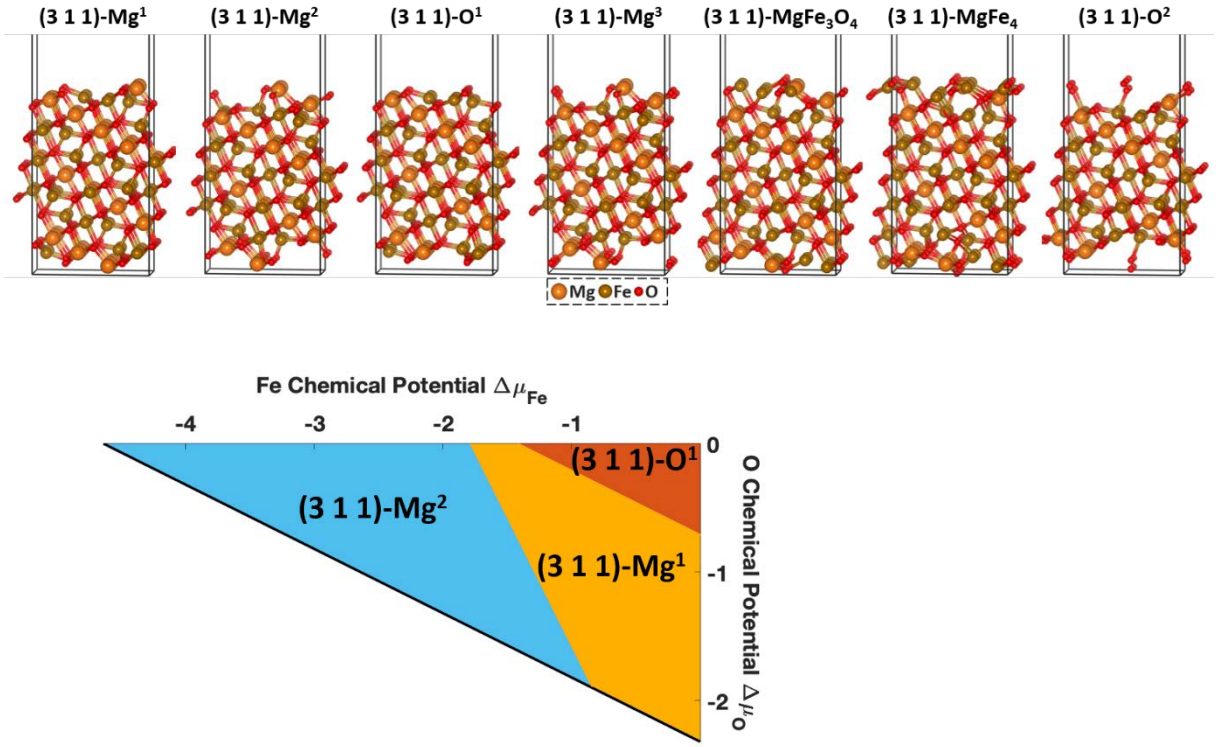

Figure S12. Surface phase diagram and structures of inverse-spinel $MgFe_2O_4$(3 1 1). Low energy surface terminations are shown for $MgFe_2O_4$ (3 1 1) in $\Delta\mu_{Fe}$ and $\Delta\mu_O$ phase space.

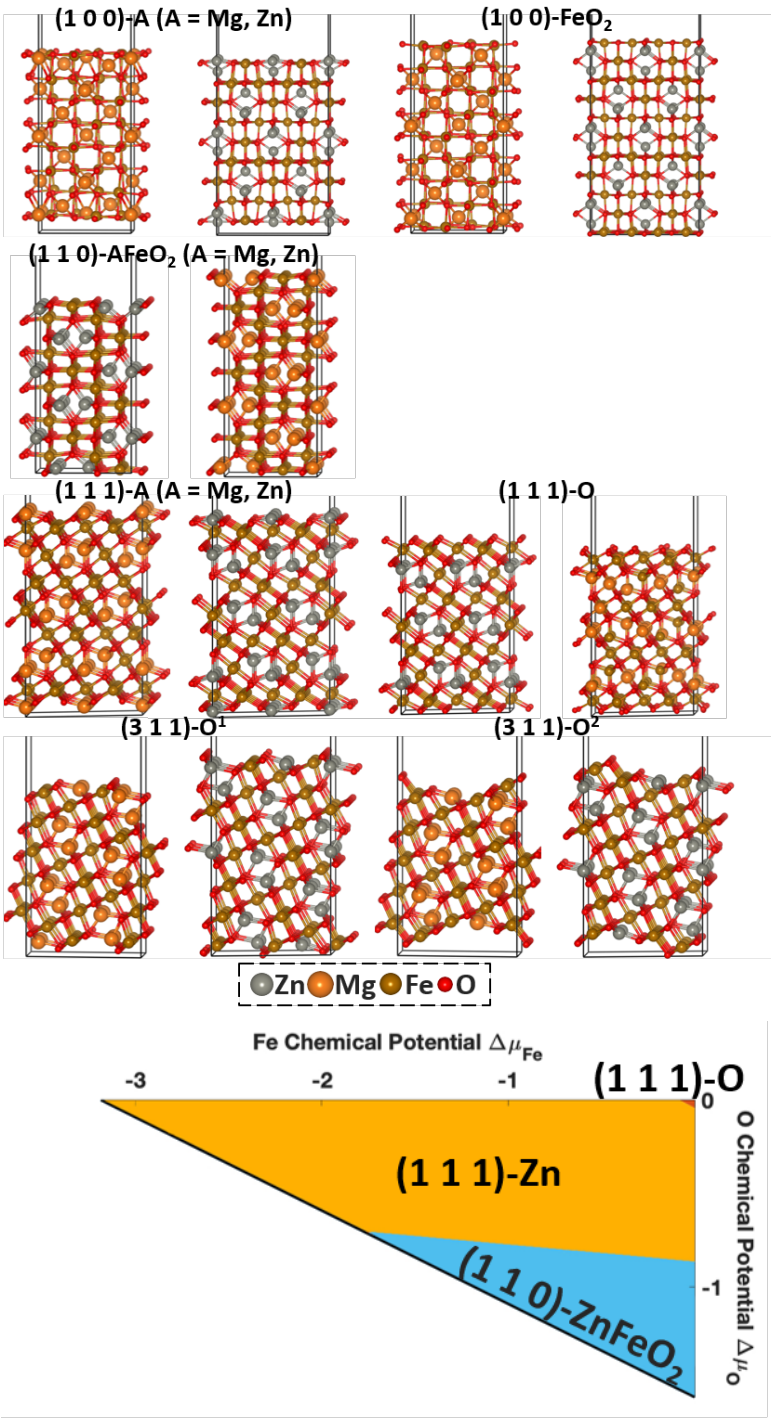

Figure S13. Phase diagram of $ZnFe_2O_4$ (1 0 0), (1 1 0), (1 1 1) and (3 1 1) surfaces[2b] and the corresponding structures of stable terminations in comparison with normal-spinel $MgFe_2O_4$.

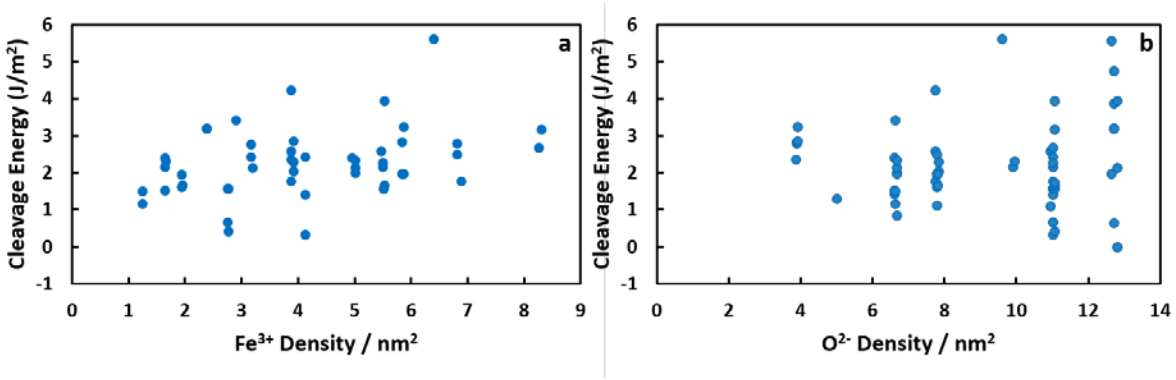

Figure S14. Correlation between the cleave energy in J/m^2 and density in nm^{-2} of Fe^{3+} (a) or O^{2-} (b) exposed to the surface.